Failed remyelination of the nonhuman primate optic nerve leads to axon degeneration, retinal damages, and visual dysfunction

Nadège Sarrazin[a], Estelle Chavret-Reculon[a], Corinne Bachelin[a], Mehdi Felfli[a], Rafik Arab[a], Sophie Gilardeau[a], Elena Brazhnikova[b], Elisabeth Dubus[b], Lydia Yaha-Cherif[a], Jean Lorenceau[c], Serge Picaud[b], Serge Rosolen[b,d], Pierre Moissonnier[e], Pierre Pouget[a], and Anne Baron-Van Evercooren[a,1]

[a]Institut du Cerveau, Sorbonne Université, INSERM, CNRS, F-75013 Paris, France; [b]Institut de la Vision, Sorbonne Université, INSERM, CNRS, F-75012 Paris, France; [c]Integrative Neuroscience and Cognition Center, Université de Paris, CNRS, F-75006 Paris, France; [d]Clinique Vétérinaire Voltaire, F-92600 Asnières-sur-Seine, France; and [e]Vet AgroSup, F-69280 Marcy-l'Étoile, France

Edited by Lawrence Steinman, Departments of Neurology & Neurological Sciences, and Pediatrics, Stanford University, Stanford, CA; received September 3, 2021; accepted January 6, 2022

White matter disorders of the central nervous system (CNS), such as multiple sclerosis (MS), lead to failure of nerve conduction and long-lasting neurological disabilities affecting a variety of sensory and motor systems, including vision. While most disease-modifying therapies target the immune and inflammatory response, the promotion of remyelination has become a new therapeutic avenue to prevent neuronal degeneration and promote recovery. Most of these strategies have been developed in short-lived rodent models of demyelination, which spontaneously repair and do not reflect the size, organization, and biology of the human CNS. Thus, well-defined nonhuman primate models are required to efficiently advance therapeutic approaches for patients. Here, we followed the consequence of long-term toxin-induced demyelination of the macaque optic nerve on remyelination and axon preservation, as well as its impact on visual functions. Findings from oculomotor behavior, ophthalmic examination, electrophysiology, and retinal imaging indicate visual impairment involving the optic nerve and retina. These visual dysfunctions fully correlated at the anatomical level, with sustained optic nerve demyelination, axonal degeneration, and alterations of the inner retinal layers. This nonhuman primate model of chronic optic nerve demyelination associated with axonal degeneration and visual dysfunction, recapitulates several key features of MS lesions and should be instrumental in providing the missing link to translate emerging repair promyelinating/neuroprotective therapies to the clinic for myelin disorders, such as MS.

demyelination | nonhuman primate | optic nerve | visual dysfunction

White matter disorders are a large group of neurological diseases of various origins. Those affecting the central nervous system (CNS), such as multiple sclerosis (MS), lead to failure of nerve conduction, axon degeneration, and result in long-lasting neurological disabilities and tissue atrophy (1). The loss of myelin and healthy axons are believed to be responsible for irreversible damages, which affect a variety of sensory and motor systems, including vision. In MS, 70% of patients are affected with optic neuritis. It can manifest in an acute episode with decreased vision that can recover over several weeks in the majority of patients, while permanent visual symptoms persist in 40 to 60% of patients (2, 3). Chronic optic neuritis can lead to significant optic nerve atrophy and retinal alterations, affecting mainly the retinal inner layers, including the retinal nerve fiber and ganglion cell layers (4). Several visual assays, including visual fields (VF) (5), pupillary responses to luminance and color (pupillary light reflex, PLR) (6), electroretinograms (ERG) (7), optical coherence tomography (OCT) (4, 8), and visual evoked potential (VEP) (9–11) are routinely performed to assess noninvasively the anatomical and electrophysiological perturbations of visual functions in MS. While functional recovery was reported in some patients (9), the lack of anatomical–electrophysiological correlation has prevented to attribute directly these improvements to remyelination or other regenerative processes.

Animal models of demyelination induced by toxins, such as lyso-phosphatidylcholine (LPC), are suitable for studying the mechanisms of demyelination/remyelination and developing approaches aimed at promoting CNS remyelination, as they show little inflammation and, therefore, provide means to assay directly the effect of a therapy on remyelination. However, most of these models are developed in short-lived rodents and spontaneously repair, thus lacking the long-lasting progressive degenerative disease context of MS. Besides, these models do not reflect the size or complex organization of the human primate CNS (12). They do not inform on the biology of primate cells, which differs from rodents (13, 14), nor on the security, toxicity, and long-term efficacy of cell- or compound-based promyelinating/neuroprotective therapies. Thus, experiments in long-lived nonhuman primates appear an essential step toward clinical trials.

IMMUNOLOGY AND INFLAMMATION

Significance

Promotion of remyelination has become a new therapeutic avenue to prevent neuronal degeneration and promote recovery in white matter diseases, such as multiple sclerosis (MS). To date most of these strategies have been developed in short-lived rodent models of demyelination, which spontaneously repair. Well-defined nonhuman primate models closer to man would allow us to efficiently advance therapeutic approaches. Here we present a nonhuman primate model of optic nerve demyelination that recapitulates several features of MS lesions. The model leads to failed remyelination, associated with progressive axonal degeneration and visual dysfunction, thus providing the missing link to translate emerging preclinical therapies to the clinic for myelin disorders such as MS.

Author contributions: N.S. and A.B.-V.E. designed research; N.S., E.C.-R., S.G., E.B., E.D., S.R., and P.M. performed research; N.S., E.C.-R., C.B., M.F., R.A., J.L., S.P., S.R., P.M., P.P., and A.B.-V.E. contributed new reagents/analytic tools; N.S., E.C.-R., C.B., M.F., R.A., E.B., L.Y.-C., J.L., S.R., P.P., and A.B.-V.E. analyzed data; N.S., E.C.-R., E.B., J.L., S.R., and A.B.-V.E. wrote the paper; J.L. and P.P. critically reviewed the manuscript; and A.B.-V.E. supervised research and handled funding.

The authors declare no competing interest.

This article is a PNAS Direct Submission.

This article is distributed under Creative Commons Attribution-NonCommercial-NoDerivatives License 4.0 (CC BY-NC-ND).

[1]To whom correspondence may be addressed. Email: anne.baron@upmc.fr.

This article contains supporting information online at http://www.pnas.org/lookup/suppl/doi:10.1073/pnas.2115973119/-/DCSupplemental.

Published March 2, 2022.

While promoting remyelination may prevent axon degeneration, only a few promyelination strategies have been translated to the clinic (15,16). One of the roadblocks is the absence of studies addressing the clinical benefit of promyelination approaches that could be applied to the clinic (17). A positive correlation between changes in VEP parameters and the degree of demyelination/remyelination was established in rodents (18–21), cats (22), and dogs (23), and exploited successfully to follow promyelination therapies in rodents (24, 25). OCT has been used to identify loss of optic nerve and retinal damages in animal models of myelin disorders as well (23, 26). While used seldomly in nonhuman primates (27), none of these clinical assays were exploited to monitor the impact of optic nerve demyelination in nonhuman primates.

We previously demonstrated that LPC injection in the macaque optic nerve induced demyelination with fair axon preservation but little remyelination up to 2 mo post demyelination (28). Taking advantage of the fact that nonhuman primates are long-lived and are able to perform several tasks awake, as do humans, we questioned whether this model could be used to follow the consequence of long-term demyelination on axon preservation, and whether multimodal noninvasive assays, such as VF, VEP, OCT, and PLR could be instrumental to follow/predict the functional and anatomical outcome of optic nerve demyelination. Using multidisciplinary approaches, we provide compelling evidence that LPC-induced demyelination of the macaque optic nerve leads to modified VF, VEP, PLR, and altered inner retinal layers, but preserved photoreceptors based on OCT and ERG. These clinical and functional anomalies were correlated at the histological level with failed remyelination and progressive optic nerve axon loss, followed by neuronal and fiber loss of the inner retinal layers. The postmortem validation of OCT, VEP, and PLR as pertinent markers of optic nerve demyelination/degeneration could further help the translation of therapeutic strategies toward the clinic for myelin diseases associated with long-term demyelination of the optic nerve.

Results

The impact of LPC-induced demyelination of the optic nerve on visual functions was studied using psycho-physic (VF), electrophysiologic (VEP, ERG), physiologic (PLR), and anatomic (OCT) tools. As saline and LPC injections could not be performed in the same animal for ethical reasons, we compared responses of the left eye corresponding to the LPC-injected optic nerve (LPC-ON) with that of the right fellow eye corresponding to the noninjected optic nerve (C-ON). Data were further correlated with postmortem analysis of the optic nerves and associated retinas of the same subjects (*SI Appendix*, Table S1).

Altered VF Sensitivity. Measuring VF sensitivity is long and challenging with awake monkeys. Therefore, we developed an in-house method relying on analyzing the latencies of saccades toward targets presented at a series of central and eccentric locations. Indeed, visual defects resulting in unseen or poorly seen targets are expected to entail long saccadic latencies, no saccade at all, or an erratic oculomotor behavior. A gaze-contingent display that triggers the successive presentations of the visual targets was used to analyze the saccadic latencies (the time for each eye to reach the new target in monocular and binocular conditions). Although this method does not directly evaluate VF sensitivity, it proved useful to identify functional VF defects consecutive to the LPC-induced demyelination (Fig. 1*A* and *SI Appendix*, Fig. S1*A* and Table S2). Statistical analysis showed a significant effect of time (***P = 1.23e-10) as well as a significant interaction time:eye (***P < 2e-16). While global mean saccade latencies between C-ON and LPC-ON did not differ significantly before lesion, they changed only slightly after lesion for the C-ON compared to the LPC-ON corresponding eye. Post hoc analysis per time point showed a significant increase in the mean saccade latencies for the LPC-ON compared to the C-ON for each time point post-LPC. As the latencies measured herein corresponded to the time between the current fixation and the fixation of a next target, these LPC-ON long latencies presumably reflect both the time required to search for the target with residual visual sensitivity, as well as the increased latency due to optic nerve degeneration. The large latency differences indicate that the LPC-induced lesion triggered important visual deficits, suggestive of retinal modifications.

Delayed VEP Latencies. To ascertain that LPC entailed visual deficits, and not the oculomotor system, we further used VEP as an objective measure of the visual pathway function. In particular, we used flash VEP and pattern reversal checkerboard-evoked potentials on awake animals to mimic as closely as possible the visual assays performed on human subjects. The control macaque VEP recorded from the scalp was characterized by wavelets that preceded a major peak around 80 ms. While changes in waveforms and amplitudes, were observed for all subjects in response to D15, D30, and D60 checkerboard, and were quite heterogeneous, we focused our analysis on P80 latency responses for D15 and D30. First, we examined P80 latency responses to the D15 checkerboard in binocular conditions at 1, 3, 5, and 9 mo post-LPC. While three animals showed stable binocular responses pre- and post-LPC, two of them had disturbed binocular responses, suggesting that their C-ON was unable to compensate for the LPC-ON. (Fig. 1*B*). Next, we analyzed D15 VEP responses for those animals with stable binocular responses in the monocular condition (Fig. 1 *C* and *D*). Statistical analysis showed a significant effect of time (*P = 0.0104), as well as a significant interaction time:eye (***P = 1.05e-05). Post hoc analysis (*SI Appendix*, Table S3) showed that prelesion average VEP latencies did not differ significantly between both eyes. While after lesion, VEP latencies remained stable for C-ON, they increased significantly for the LPC-ON corresponding eye. Moreover, analysis at each time point, indicated a statistically prolonged latency for the LPC-ON corresponding eye relative to C-ON and as early as 1 mo post-LPC. Latency differences were also observed for responses to the D30 checkerboard (*SI Appendix*, Fig. S1*B* and Table S3).

Abnormal N2 latency responses to red (Fig. 1 *E* and *F* and *SI Appendix*, Table S3) and blue flashes (*SI Appendix*, Fig. S1*C* and Table S3) were also analyzed. A significant effect of time (***P = 0.000128) as well as a significant time:eye interaction (***P = 3.92e-07) was found for red flashes. Post hoc analysis indicated that prelesion averaged VEP latencies responses to red flashes, did not differ significantly between C-ON and LPC-ON. However, they increased markedly post-LPC for the LPC-ON corresponding eye, compared to C-ON. Moreover, post hoc analysis for each time-point showed that N2 latencies were prolonged for the LPC-ON corresponding eye over the C-ON corresponding fellow eye as off 1 mo post-LPC for all five animals, with significant mean value differences for all time points post-LPC. Statistical differences were also observed with blue flashes at 1 and 3 mo post-LPC, but not at later times. Thus, analysis of VEPs (checkerboard and flashes) indicates that axons and their cell bodies are involved in visual impairment.

Changes in PLR Responses. PLR involves a short pathway, from the retina to the ciliary ganglions innervating the iris sphincter, with relays in the PON and the Edinger–Westphal nucleus. Given that PLR is altered in optic neuritis, and used as a measure of optic nerve dysfunction, PLR responses were measured before and after lesion. First, we analyzed PLR responses to

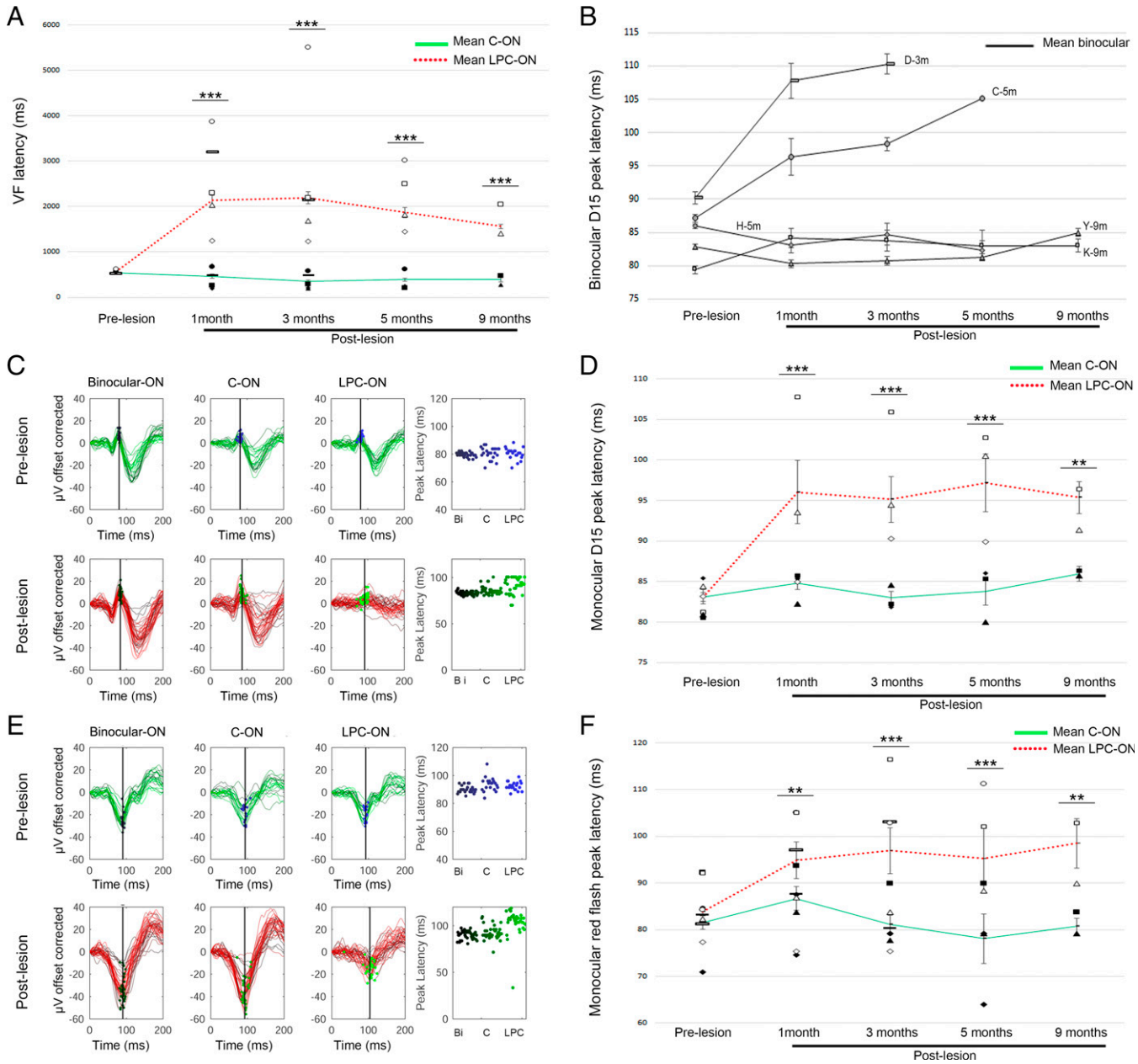

Fig. 1. Longitudinal evolution of VF and VEPs in response to optic nerve LPC-induced demyelination. (*A*) Diagram of VF latencies of C-ON and LPC-ON corresponding eyes. Differences between pre- and post-LPC are not significant for C-ON ($n = 5$, $P = 0.373$) and LPC-ON ($n = 5$, $P < 0.662$). Differences between eyes are significant from 1 mo and 3 mo, $n = 5$; 5 mo $n = 4$; 9 mo, $n = 2$ ($P < 0.001$). (*B*) Diagram of D15 checkerboard latencies in binocular conditions (1-, 3 mo, $n = 5$; 5 mo $n = 4$; 9 mo, $n = 2$). Two of five subjects have altered D15 latencies in binocular conditions. (*C*) Representative curves of D15 checkerboard, P80 peak in binocular and monocular conditions for one subject. (*D*) Diagram of D15 checkerboard latencies in monocular conditions. Differences between pre- and post-LPC are significant for LPC-ON only ($n = 3$, $P = 0.056$). Differences between eyes are significant at 1, 3, 5 ($n = 3$, $P < 0.0001$), and 9 ($n = 2$, $P = 0.0053$) mo. (*E*) Representative curves of red flashes, N2 peak in the binocular and monocular conditions for one subject. (*F*) Diagram of red flashes N2 latencies in monocular conditions for C-ON and LPC-ON. Differences between pre- and post-LPC are significant for LPC-ON only ($n = 3$, $P = 0.049$). Differences are significant at 1 ($n = 3$, $P = 0.0025$), 3 ($n = 3$, $P < 0.0001$), 5 ($n = 3$, $P < 0.0003$), and 9 ($n = 2$, $P = 0.0092$) mo post-LPC. In *D* and *F*, full symbols represent base-line data and empty symbols postdemyelination data; subject correspondence is as follows: squares, K-9m; circles, C5-m; rectangles, D-3m; diamonds, H-5m; triangles, Y-9m. Asterisks (*) indicate the significant difference between C-ON and LPC-ON for a given @ time point. $^{**}P < 0.01$, $^{***}P < 0.001$.

increasing intensities of blue and decreasing intensities of red flashes prior to LPC injection. We focused on the C2-negative peak as a measure of pupillary maximal constriction, followed by postillumination pupillary reflex (PIPR, blue flashes only) as a measure of PIPR or partial recovery to a normal pupil state. We constructed an irradiance-response curve to 1-s light exposure for each animal in nonlesion condition (Fig. 2*A*). Pupil diameter changed dynamically over the entire range of irradiance, with optimal constriction (C2) from 2.01 logCd/m^2 and PIPR responses detectable in blue conditions only.

Next, we compared the pupillary responses of the C-ON and LPC-ON corresponding eyes over time at 2.01 logCd/m^2. C2 (Fig. 2 *B* and *D*) and PIPR (Fig. 2*C*) values expressed in percentage of baseline in nonstimulated conditions did not differ significantly pre-LPC between C-ON and LPC-ON in blue or red stimulation (*SI Appendix*, Table S4). Moreover, lesion

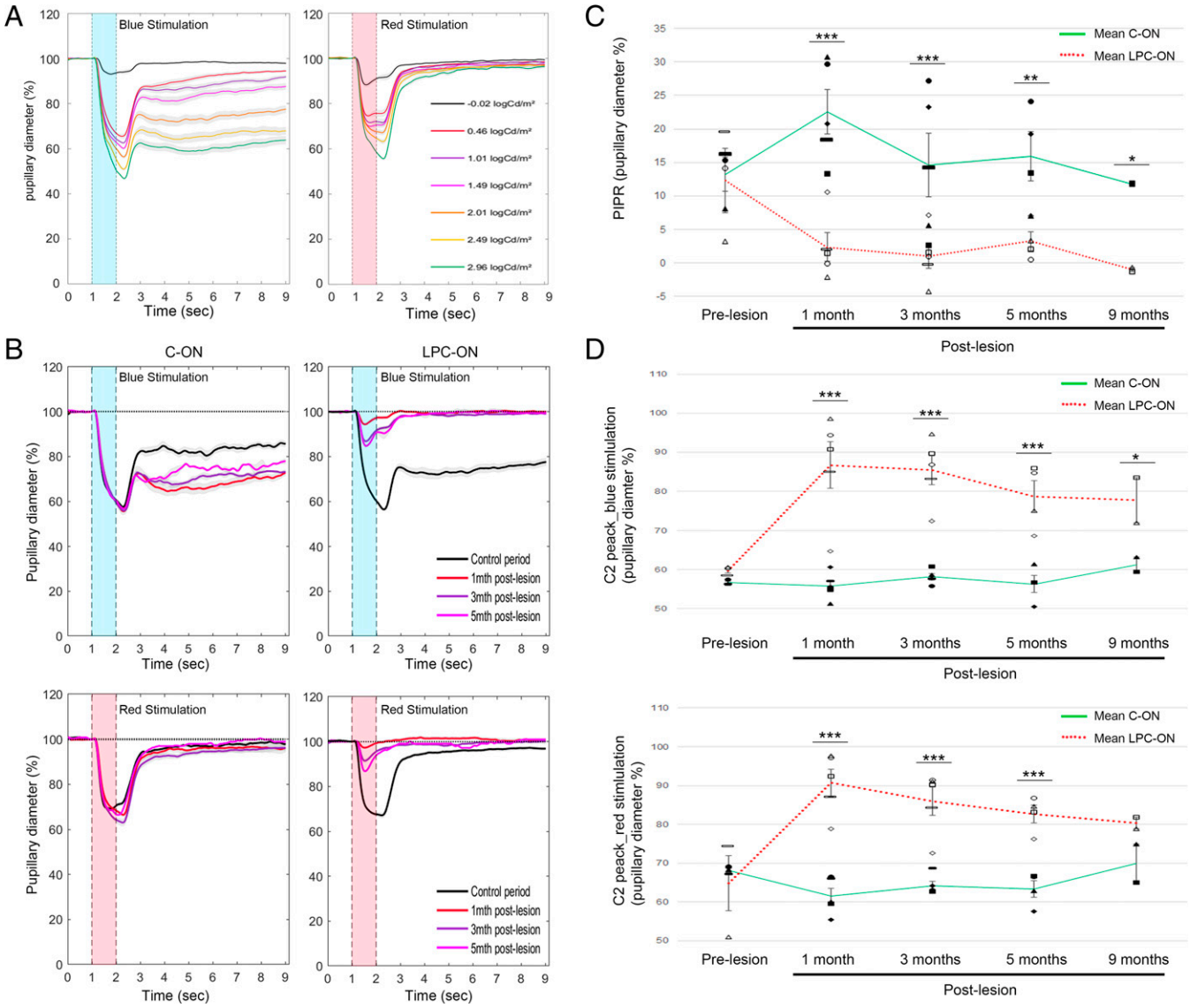

Fig. 2. Longitudinal lesion-induced changes in PLR. (*A*) Pupillary responses after blue or red flashes at different intensities. (*B*) Representative pupillary responses to 2.01 log Cd/m^2 post-LPC after blue (*Upper*) and red (*Lower*) stimulation. (*C*) Diagram of PIPR in response to blue stimulation. Differences between pre- and post-LPC are significant for LPC-ON only at 1 (n = 5, P < 0.00001), 3 (n = 5, P < 0.0001), 5 (n = 3, P < 0.001), and 9 (n = 2, P = 0.03) mo. (*D*) Diagram of C2 peak in response to blue (*Upper*) and red (*Lower*) stimulation. Differences between pre- and post-LPC are significant for LPC-ON only. Differences between eyes are significant at 1, 3 (n = 5, P < 0.00001), 5 (n = 3, P < 0.00001), and 9 (n = 2, P < 0.01) mo in blue condition. In red conditions, differences between eyes are significant at 1, 3 (n = 5, P < 0.001), and 5 (n = 3, P < 0.001) mo post-LPC. In *B* and *C*, full symbols represent base-line data and empty symbols postdemyelination data; subject correspondence is as follows: squares, K-9m; circles, C5-m; rectangles, D-3m; diamonds, H-5m; triangles, Y-9m. Asterisks (*) indicate the significant difference between C-ON and LPC-ON for a given time point. *P < 0.05, **P < 0.01, ***P < 0.001.

induction in the LPC-ON had no impact on the C-ON since C2 and PIPR values of the control eye did not change pre- and post-LPC in response to blue and red stimulations. Statistical analysis of pupillary constriction based on C2 values showed a significant effect of time, as well as a significant interaction time: eye for blue (time, P = 0.001550; time:eye, P = 0.002528) and red flashes (time, P = 0.004032, time:eye, P = 4.546e-05). Pupillary constriction decreased at all times post-LPC in the LPC-ON in response to blue flashes and red flashes. PIPR responses of the LPC-ON corresponding eye, detectable in blue conditions only, decreased dramatically at all time points post-LPC. Thus, the lesion affected both the maximum constriction and PIPR.

Preservation of ERGs. To further investigate whether LPC-induced demyelination of the optic nerve did affect the most outer retinal layers, we performed ERG before and after LPC injection and compared the ERG responses of the LPC injected side over the noninjected side. Wave parameter's mean values (± SD) before (n = 3) and after LPC injection of the optic nerve (n = 4) are presented in *SI Appendix*, Table S5 and illustrated Fig. 3*A*. For all animals, each eye, and each condition, ERG responses were discernable from the background noise. Before LPC, in all stimulation conditions, ANOVA analysis (P < 0.05) did not yield any difference between the right C-ON and left LPC-ON corresponding eyes. Amplitudes slightly decreased post-LPC compared to values pre-LPC in both eyes. Moreover, mixed ERG waves and normal photopic and scotopic A and B waves were unchanged after LPC-induced demyelination compared to the internal control right eye and pre-LPC left eye. These observations predict that the photoreceptors (cone and rods) and their outputs are not affected by the LPC-induced demyelination.

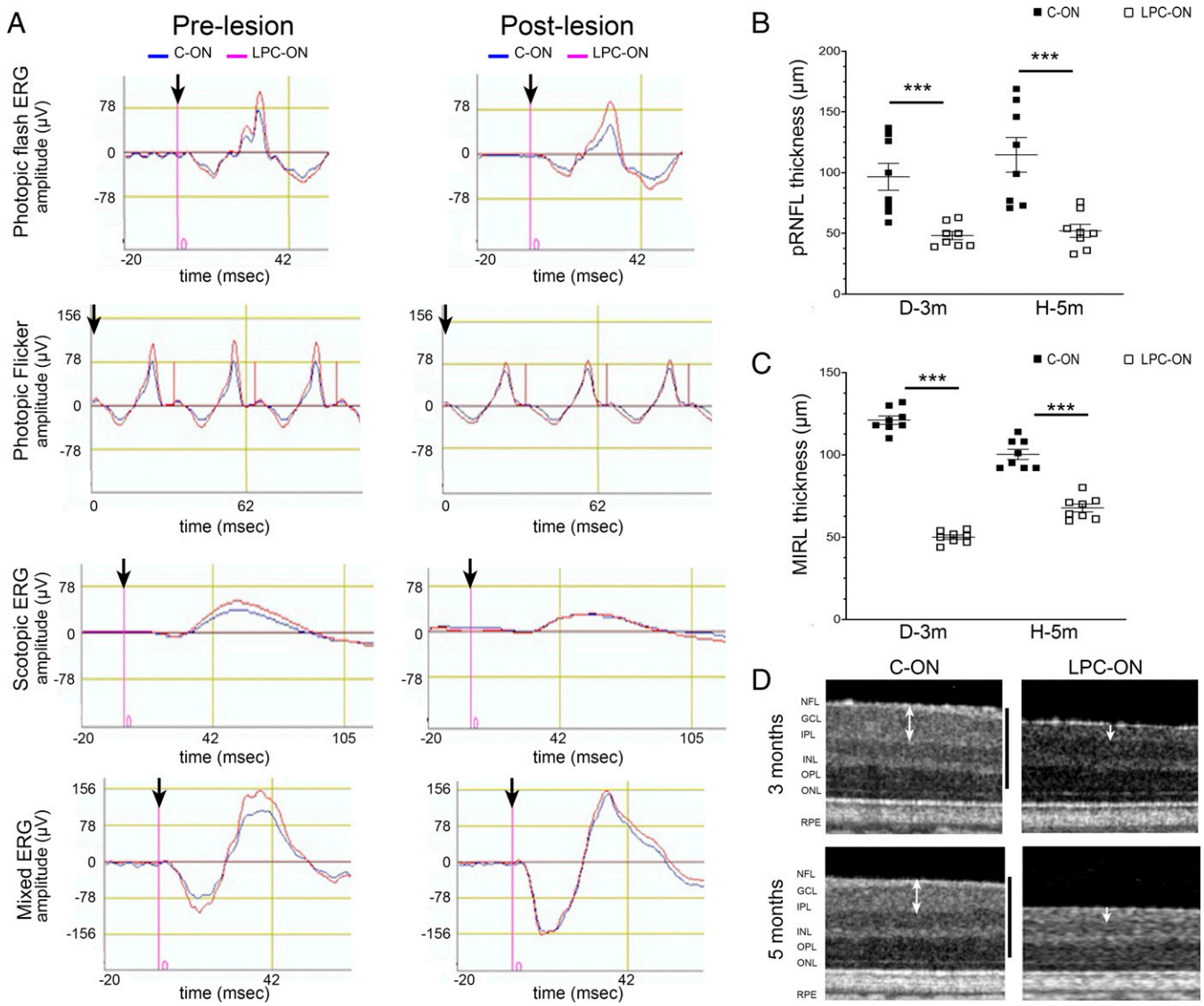

Fig. 3. Evaluation of lesion-induced retinal changes by ERG and OCT. (*A*) Representative ERG waves showing Mixed ERG waves and normal photopic and scotopic A and B waves, which are unchanged pre- and post-LPC in C-ON (blue), compared to LPC-ON. The black arrow represents the flash onset. (*B* and *C*) The average thickness of (*B*) pRNFL and (*C*) MIRL thickness of retinas corresponding to C-ON (full columns) and LPC-ON (empty columns) at 3 (n = 1) and 5 (n = 1) mo post-LPC. (*D*) MIRL of retinas corresponding to the C-ON, and LPC-ON at 3 and 5 mo post-LPC injection. White arrows point to macular inner layer thickness. Data are the mean ± SEM for each monkey, t test ***$P < 0.001$. (Scale bars in *D*, 250 µm.)

OCT Imaging Changes. Finally, we used spectral domain OCT (SD-OCT) to assess the effects of LPC on the peri-papillary retinal nerve fiber layer (pRNFL) thickness and the macular inner retinal layer (MIRL) thickness. OCT measurements were performed before killing at 3 (n = 1) and 5 (n = 1) mo post-LPC injection of the ON.

The average pRNFL thickness measured by RNFL 3.45 scanning post-LPC was 50.19 ± 1.94 µm for the LPC-ON corresponding eye, compared to the average pRNFL thickness of 105.69 ± 9.06 µm for the internal C-ON corresponding eye (n = 2), respectively, the difference being of 53% (D-3m: P = 0.0009; H-5m: P = 0.001) (Fig. 3*B*). The MIRL was then automatically calculated on the superior, nasal, inferior, and temporal quadrants in the Early Treatment Diabetic Retinopathy Study (ETDRS)-type areas by the retina map scan pattern (Fig. 3*C*). The average MIRL thickness at 3 and 5 mo after injection from two LPC-ON corresponding eyes was 58.53 ± 9.1 µm compared to 110.69 ±10.4 µm in the two C-ON, the difference of MIRL thickness being of 52% (D-3m: P = 5.4e-13; H-5m: P = 9e-07). Analysis of MIRL thickness at 3 and 5 mo post-LPC, showed a thickness decline of all measured macular areas (Fig. 3*D*). Altogether, the OCT data indicate that LPC-induced demyelination of the optic nerve worsens, in time and space, the retinal thickness of the LPC-ON corresponding eye without affecting the retina of the C-ON corresponding fellow eye.

The assessment of the optic nerve head parameters with the glaucoma scan mode showed a significant increase in the cup-to-disk (C/D) area ratio (+39% at 3 mo and 88% at 5 mo post-LPC) and decrease in the rim area (−57% at 3 mo post-LPC and −45% at 5 mo post-LPC), most likely reflecting optic nerve damage, including both demyelination and axonal loss (*SI Appendix*, Table S6).

Immunohistological Characterization of Optic Nerve Lesions. Next, we analyzed the long-term effect of LPC-induced demyelination in the optic nerve by immunohistochemistry and electron

microscopy on cross-sections of the LPC-ON and C-ON of the same animals (*SI Appendix*, Table S1) at 3, 5, and 9 mo post-LPC injection.

Immunohistochemical analysis of the optic nerve showed a decrease in the nerve section area of 2-, 1.7-, and 1.9-fold in the LPC-ON over C-ON at 3, 5, and 9 mo post-LPC, respectively (Fig. 4 *A–C*). Although the global architecture of the LPC-ON appeared to be well preserved, gaps between bundles occurred at the latest time-point (9 mo). Immunolabeling for myelin basic protein (MBP) revealed that demyelination was extensive with a decrease in the MBP^+ area of 1.3-, 1.9-, and 2.6-fold in the LPC-ON over C-ON at 3, 5, and 9 mo post-LPC (Fig. 4 *D–F*). Immunohistochemistry for neurofilaments (NF) to detect NF in axons, showed only partial preservation of axons in the LPC-ON, with a decrease in the number of NF^+ axons of 1.2-, 1.3-, and 1.7-fold in the LPC-ON over C-ON at 3, 5, and 9 mo post-LPC (Fig. 4 *G–I*). Double immunodetection of MBP and NF showed that axons were mostly devoid of MBP^+ myelin in the core of the lesion, but enwrapped by MBP^+ donut-shaped structures at the lesion edge (Fig. 4*H*), suggesting the presence of remyelinated axons.

As remyelination is a complex process involving multiple glial partners, we analyzed the cellular dynamics of the lesion in the C-ON and LPC-ON. Hoechst labeling to detect all cell nuclei, showed a significant increase in cell density of 1.5-, 1.3-, and 1.4-fold in lesions of the LPC-ON over control, at 3, 5, and 9 mo post-LPC (*SI Appendix*, Fig. S2 *A*, *B′*, and *G*). In rodents, oligodendrocyte progenitors (15) and mature oligodendrocytes (29–31) are involved in the process of remyelination. Therefore, we analyzed the oligodendroglial compartment performing double immunolabeling for Olig2 as a general marker of the oligodendroglial lineage and CC1 as a marker of mature oligodendrocytes (Fig. 5). While $Olig2^+$ cells were present in all lesions, their number decreased 5.1-, 26.2-, and 1.1-fold in lesions of the LPC-ON compared to the C-ON at 3, 5, and 9 mo post-LPC (Fig. 5 *A–E*). This decrease in $Olig2^+$ cells involved immature $Olig2^+/CC1^-$ and mature $Olig2^+/CC1^+$ oligodendroglial cells (Fig. 5 *F* and *G*). Immunolabeling for the proliferation marker K_i67 and OLIG2, and Hoechst dye showed that few $Hoechst^+$ or $Olig2^+$ cells were K_i67^+ within the lesion, including its border at any time point, suggesting their quiescence. Immunodetection of myeloid cells (CNS-resident microglia and blood-derived monocytes) with the Iba1 marker pointed to a significant increase in $Iba1^+$ cell density of 2-, 2.7-, and 2.7-fold in the LPC-ON over C-ON at 3, 5, and 9 mo post-LPC (*SI Appendix*, Fig. S2*H*). Interestingly while $Iba1^+$ cells were homogeneously dispersed in the C-ON and LPC-

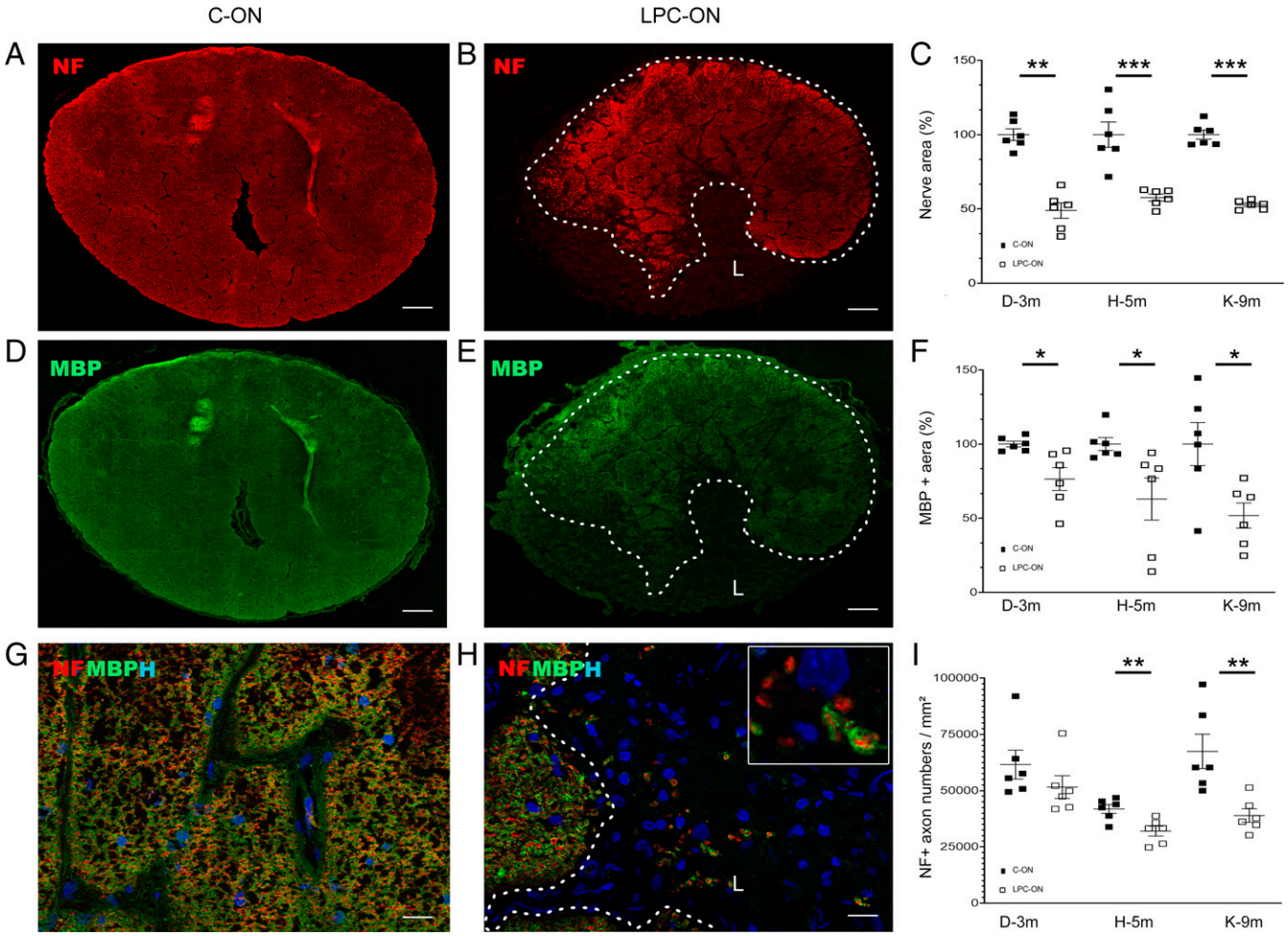

Fig. 4. Immunohistological characterization of axons and myelin in 9 mo post-LPC C-ON (*A*, *D*, and *G*) and LPC-ON (*B*, *E*, and *H*) representative cross-sections. (*A–H*) Immunodetection of axons (NF, red) and myelin (MBP, green) viewed in single (*A*, *B*, *D*, *E*) or combined (*G* and *H*) channels. Dotted lines indicate the lesion (L) limit. (*C*, *F*, and *I*) Quantifications of the nerve section area (*C*), MBP^+ myelin area (*F*), and NF^+ structures (*I*) in C-ON and LPC-ON at 3 (n = 1), 5 (n = 1), and 9 (n = 1) mo post-LPC. Nerve shrinkage correlates with myelin and axonal loss. *Inset* in *H* illustrates the presence of axons enwrapped by MBP^+ myelin at the lesion border. For each subject, data for the LPC-ON (empty squares) are expressed in *C* and *F* as a percentage of the corresponding C-ON fellow nerve values (full squares) and axon number/mm^2 in *I*. Data are the mean ± SEM, t test $*P < 0.05$, $**P < 0.01$, $***P < 0.001$. (Scale bars: 200 μm in *A*, *B*, *D*, and *E*; 20 μm in *G* and *H*, *Inset* in *H*: 5 μm.)

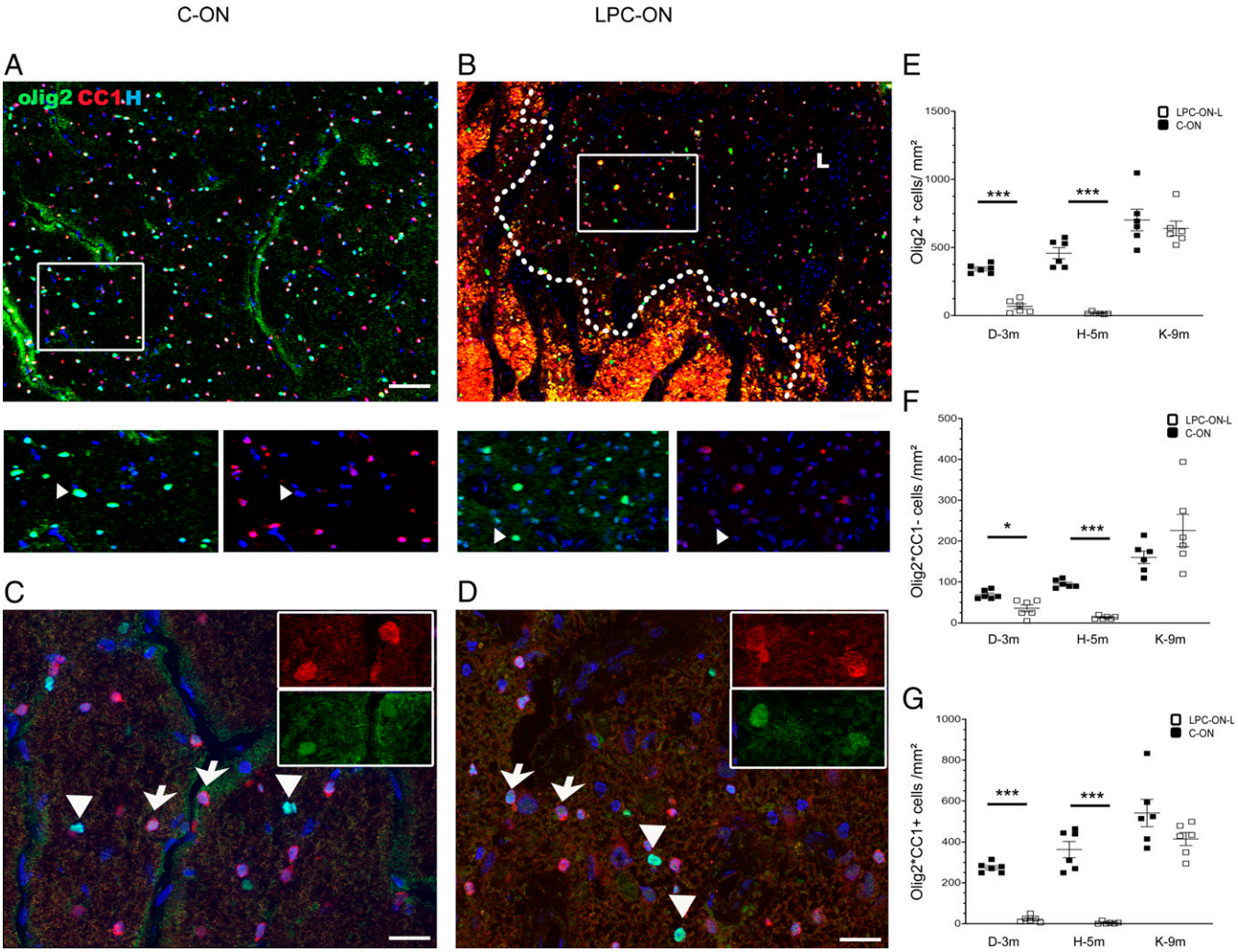

Fig. 5. Immunohistological analysis of the optic nerve oligodendroglial populations. Representative 9 mo post-LPC cross-sections of C-ON (*A* and *C*) and LPC-ON (*B* and *D*) stained for Olig2 (green), CC1 (red), and Hoechst (H, blue). (*A* and *B*) General views of the parenchyma. Dotted lines indicate the lesion (L) limits. (*C* and *D*) Details of C-ON (*C*) and LPC-ON (*D*). *Insets* illustrate single channels. Cells express Olig2 alone (arrowheads) or with CC1 (arrows). (*E–G*) Quantifications of Olig2$^+$ (*E*), Olig2$^+$/CC1$^-$ (*F*), and Olig2$^+$/CC1$^+$ (*G*) cells/mm^2 in C-ON and LPC-ON at 3, 5, and 9 mo post-LPC. Black squares represent values for C-ON and empty squares, values of LPC-ON. Data are the mean ± SEM, *t* test $*P < 0.05$, $***P < 0.001$. (Scale bars: 100 μm in *A* and *B*; 20 μm in *C* and *D*,enlargements in *A* and *B*: 10 μm, *Inset* in *C* and *D*: 7 μm.)

ON, they had features on nonactivated microglia with ramified processes in C-ON, but of activated microglial with amoeboid shapes in the LPC-ON (*SI Appendix*, Fig. S2 *C′* and *D′*). Immunolabeling for GFAP to detect astrocytes highlighted a marked increase of GFAP$^+$ area of 2.8-, 2.2-, and 2.3-fold in the LPC-ON over C-ON at 3, 5, and 9 mo post-LPC (*SI Appendix*, Fig. S2*I*). GFAP$^+$ cells within the lesion had enlarged cell processes compared to GFAP$^+$ cells of control-ON, which were stellate with thin ramified processes (*SI Appendix*, Fig. S2 *E′* and *F′*). Double labeling for GFAP and NF indicated that GFAP reactivity concerned the whole optic nerve section, including the lesion, which was largely depleted in axons. These data indicate that both microglial cells and astrocytes contribute to the increased cellularity detected with Hoechst within the lesion.

Ultrastructural Changes of the Optic Nerve Lesions. Our previous electron microscopy data showed that demyelination of the optic nerve is achieved at 1 wk post-LPC injection, leading to healthy demyelinated axon bundles at 1, 2, and 6 wk. While attempts of axon ensheathment by oligodendrocytes were detected at 1 and 2 wk post-LPC injection, 0.4 ± 0.2% of the surviving axons in the whole lesion, was surrounded by newly formed myelin (defined by thin myelin sheaths) (28).

Presently, we analyzed the long-term consequence of LPC injection in the optic nerve at 3, 5, and 9 mo post-LPC. Semi-thin cross-sections stained for toluidine blue confirmed shrinkage of the LPC-ON nerve area, ranging from 26 to 60% of the C-ON area (Fig. 6 *A–D*). At the ultrastructural level, the C-ON harbored myelinated axon bundles separated from each other by vascular structures and perivascular astrocytes, and oligodendrocytes (Fig. 6 *A1* and *A2*). The LPC-ON was characterized by extensive demyelination. Although scaring or necrosis did not occur, the bundle organization was partially disrupted in the LPC-ON lesion. Axon depletion was more obvious in the lesion core than the rim. While astrocyte processes surrounded axon pockets at 3 mo postlesion (Fig. 6 *B1*), fibrous astrocyte processes progressively occupied the space normally occupied by axons, confirming our immunohistological observations (Fig. 6 *C1–D2* and *SI Appendix*, Fig. S3). Moreover, the denuded axons contained NFs, but became depleted in microtubules, a sign of axon sufferance (Fig. 6 *C1* and *D1*). Electron dense axo-glial contacts were also observed at later time points (*SI Appendix*, Fig. S3 *D* and *F*). Myelin-laden macrophages and

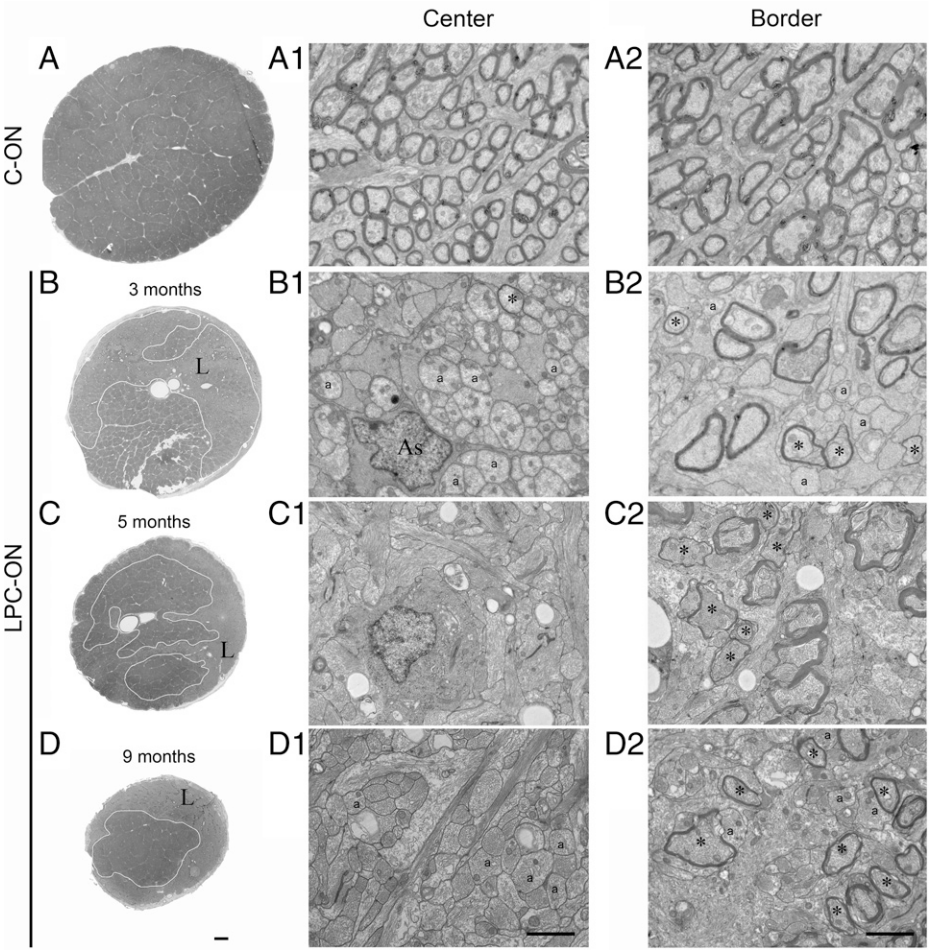

Fig. 6. Ultrastructural characterization of the C-ON (*A*, *A1*, and *A2*) and LPC-ON at 3 (*B*, *B1*, and *B2*), 5 (*C*, *C1*, and *C2*), and 9 (*D*, *D1*, and *D2*) mo post-LPC. (*A–D*) Semithin optic nerve cross-sections illustrating progressive nerve shrinkage. (*B1*, *C1*, *D1*) Ultrathin sections illustrating the center of the lesion. (*B1*) At 3 mo post-LPC, a great majority of axons survive and form clusters surrounded by astrocyte (As) processes. (*C1* and *D1*), At 5 and 9 mo post-LPC, axon clustering is followed by progressive axon loss and replacement by astrocyte processes. (*B2*, *C2*, *D2*) Ultrathin sections illustrating the border of the lesion. Thin myelin (*) identifies remyelination at the lesion rim only. (Scale bars: 200 μm in *A–D*, 2 μm in *A1–D2*.)

microglia were present mainly in the lesion rim, (*SI Appendix*, Fig. S4 *A*, *D*, and *E*). As observed by immunohistochemistry, mature (dark) and immature (light) oligodendrocytes were present at all time points in the lesion core and rim (*SI Appendix*, Fig. S4 *A* and *B*). In the rim, oligodendrocytes were sometimes in contact with axons without forming myelin. Others were surrounded by remyelinated axons (recognized by thin myelin) (Fig. 6 *B2*, *C2*, and *D2*). Remyelination was present only at the rim of the lesion. The percentage of remyelinated axons among the surviving axons at the lesion rim was similar among the different time points (12.66%, 13.39%, and 12.18% at 3, 5, and 9 mo, respectively), and only slightly increased compared to 6 wk post-LPC (28). G ratios of remyelinated axons in the LPC-ON (LPC-ON 3 mo: 0.87 ± 0.004, $P < 0.001$; 5 mo: 0.86 ± 0.006, $P = 0.001$; 9 mo: 0.86 ± 0.004, $P < 0.001$; $n = 6$ per nerve/animal) were significantly higher than C-ON (C-ON: 0.73 ± 0.009, $n = 6$ per nerve/animal) and did not seem to vary among animals (P: 0.98; 0.90; 0.99, $n = 6$ per nerve/animal). Thus, although LPC injection of the optic nerve leads to demyelination and remyelination onsets at early time points (28), it is followed by major axon loss, persisting inflammation (microglial cells and astrocytosis), and sustained demyelination at later time points.

Immunohistological Characterization of Retinas. As retinal ganglion cells (RGCs) project in the optic nerve, we examined the consequence of long-term optic nerve demyelination on the retina. First, we performed immunohistochemistry on whole-mount retinas (control and lesion side) to generate a global view of the impact of the optic nerve demyelination on the morphological status of the LPC-ON corresponding retina, and compared it to that of the C-ON (Fig. 7). Immunolabeling for NF and Brn3a, markers of NFs and RGCs, respectively, highlighted a decrease of 2-, 3.6-, and 1.5-fold in the nerve fiber layer area, as well as a decrease of 5.8-, 11.6-, and 2.4-fold in RGC density on the LPC-ON side compared to the C-ON side at 3, 5, and 9 mo post-LPC. Analysis of the RGCs versus the RNFL data indicated that RGCs were more vulnerable than RNFL with a decrease of 5.2-fold for RGC and 2.2-fold for RNFL for the LPC-ON compared to C-ON corresponding retinas.

Ultrastructural Retinal Changes. Alterations of the retina were further validated in semithin and ultrathin cross-sections of two animals killed at 5 and 9 mo post-LPC. Semithin cross-sections of the retina revealed a progressive decrease in retinal thickness post-LPC (C-ON: 310 μm; 5 mo: 260 μm; 9 mo: 200 μm) involving the innermost retinal layers of optic nerve fibers (layer 9) and RGC (layer 8) (Fig. 8). Analysis of ultrathin sections confirmed that thickness reduction concerned the retinal inner layers compartment (C-ON: 150 μm; LPC-ON 5 mo: 105 μm; 9 mo: 60 μm), including the nerve fiber and ganglion cell layers, while the outer layer thickness remained unaffected (C-ON: 160 μm; LPC-ON: 5 mo: 155 μm; 9 mo: 140 μm) (*SI Appendix*, Fig. S5). Anomalies of the retinal inner layer were further characterized at the ultrastructural level. The nerve fiber, RGC, and inner plexiform layers all showed various degrees of alterations. Axon bundles were severely disorganized in the retinal fiber layer 5 mo post-LPC, and completely vanished 9 mo post-LPC. The major loss occurred in the RGC layer at 9 mo post-LPC compared to 5 mo post-LPC. Moreover, a decrease in synaptic contacts and altered mitochondria in the synaptic endings

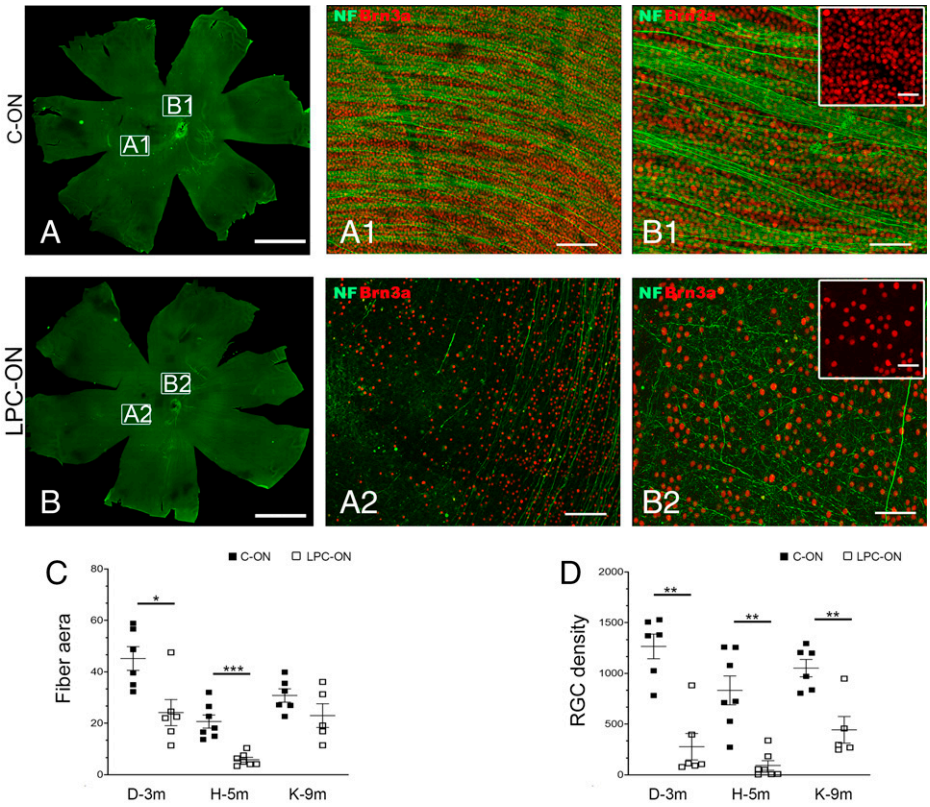

Fig. 7. Immunohistochemical characterization of the LPC-induced retinal modifications. (*A* and *B*) Immunodetection of Brn3a (red) for RGCs, and NF (green) for axons: drastic reduction of RGCs and axons in the LPC-ON corresponding retina (*B*, *B1*, and *B2*), compared to the C-ON (*A*, *A1*, *A2*) retina at 9 mo post-LPC. Boxed areas near the fovea (*A*) and optic nerve head (*B*) are magnified in *A1*, *A2*, and *B1*, *B2*, respectively. (*C* and *D*) Quantification: significant decrease in the nerve fiber area fraction (*C*) and RGC density (*D*) with time post-LPC. Data for each subject are expressed relative to the corresponding C-ON fellow nerve values (n = 1 per time point). Data are the mean ± SEM, t test $*P < 0.05$, $**P < 0.01$, $***P < 0.001$. (Scale bars: 6 mm in *A* and *B*; 50 μm in *A1*, *A2*, *B1*, *B2*; and 25 μm in the *Insets*.)

occurred in the plexiform layer and was more severe at 9 mo post-LPC compared to 5 mo post-LPC. In contrast, the retinal pigmented epithelium, photoreceptor layer, outer limiting membrane, and outer plexiform layer had a very similar morphology in the LPC-ON corresponding retinas compared to those of the C-ON. These morphological observations indicate that the LPC-induced chronic lesions of the optic nerve were associated with progressive retinal degeneration of the inner retinal layers.

Discussion

Since we initiated this work, several preclinical studies have addressed the consequences of optic nerve myelin perturbations on visual functions in rodents, dogs, and cats (18–23). Yet the relevance of these correlative studies to primates is questionable in view of several distinct differences existing between these species and primates (12). In particular, Old World monkeys have eye sizes much closer to man, visual acuity driven macula that is absent in mice and reduced in dogs, and are endowed with trichromatic vision similar to humans. Another advantage of nonhuman primates is the availability of a panel of instruments that can reveal insights into the visual system state in living rather than anesthetized conditions. VF, VEP, and PLR on awake animals can be correlated to structural assays, such as OCT and ERG, all of which are used in clinic for altered vision disorders, including MS. For example, while compression or genetically acquired hypomyelination of the optic nerve has been associated with altered VEPs in mice (18–21) and dogs (23), these assays consisted in flash recordings and were always performed on anesthetized subjects, a condition likely to modify VEP and ERG responses (32). Moreover, none of these preclinical studies addressed the functional consequences of long-term optic nerve demyelination in nonhuman primates. Combining these approaches, we show that LPC-induced demyelination of the macaque optic nerve leads to altered VF, VEP, and PLR responses but preserved ERG. PLR, and VEP were predictive of optic nerve lesions involving the RGC population, and this was confirmed both by OCT and postmortem analysis. While VEP assays address the visual pathway, PLR relates to the nonvisual pathway, which is mediated by a subset of RGC. Our data suggest that the optic nerve lesions affected both pathways. ERG predicted the absence of photoreceptor and bipolar cell involvement and thus the absence of retrograde degeneration, all of which was confirmed by postmortem analysis as well.

In clinical studies involving MS subjects, it is uncertain whether VEP alterations as a mean to assess axon conduction are correlated anatomically to optic nerve demyelination and axonal loss (33). We show that the delayed VEP responses correlated with both optic nerve demyelination and axonal loss at the histological level. In our earlier study, we showed that demyelination of the optic nerve occurs as early as 1 wk post-LPC injection and is associated with poor remyelination, despite fair axon preservation up to 2 mo post-LPC injection (28). Using the same protocol and operator, we presently show by immunohistochemistry and electron microscopy that remyelination stalls and axonal loss worsens from 3 mo post-LPC (*SI Appendix*, Fig. S6). Thus, the early phase of demyelination/remyelination with minor axonal loss is followed by a second phase of chronic demyelination and axon degeneration. Interestingly, delayed VEP responses appeared as early as 1 mo post-LPC, a time at which the majority of axons were demyelinated and appeared healthy, suggesting that the early VEP response is caused by demyelination rather than axonal loss. We also show at the histological level that the second phase (5 and 9 mo post-LPC) is characterized by the progressive replacement of axons by astrocyte processes and persisting demyelination. Interestingly, VEP latency restoration or aggravation overtime was not observed. While the absence of VEP restoration is consistent with the absence of axon regeneration and remyelination, the absence of VEP worsening could be

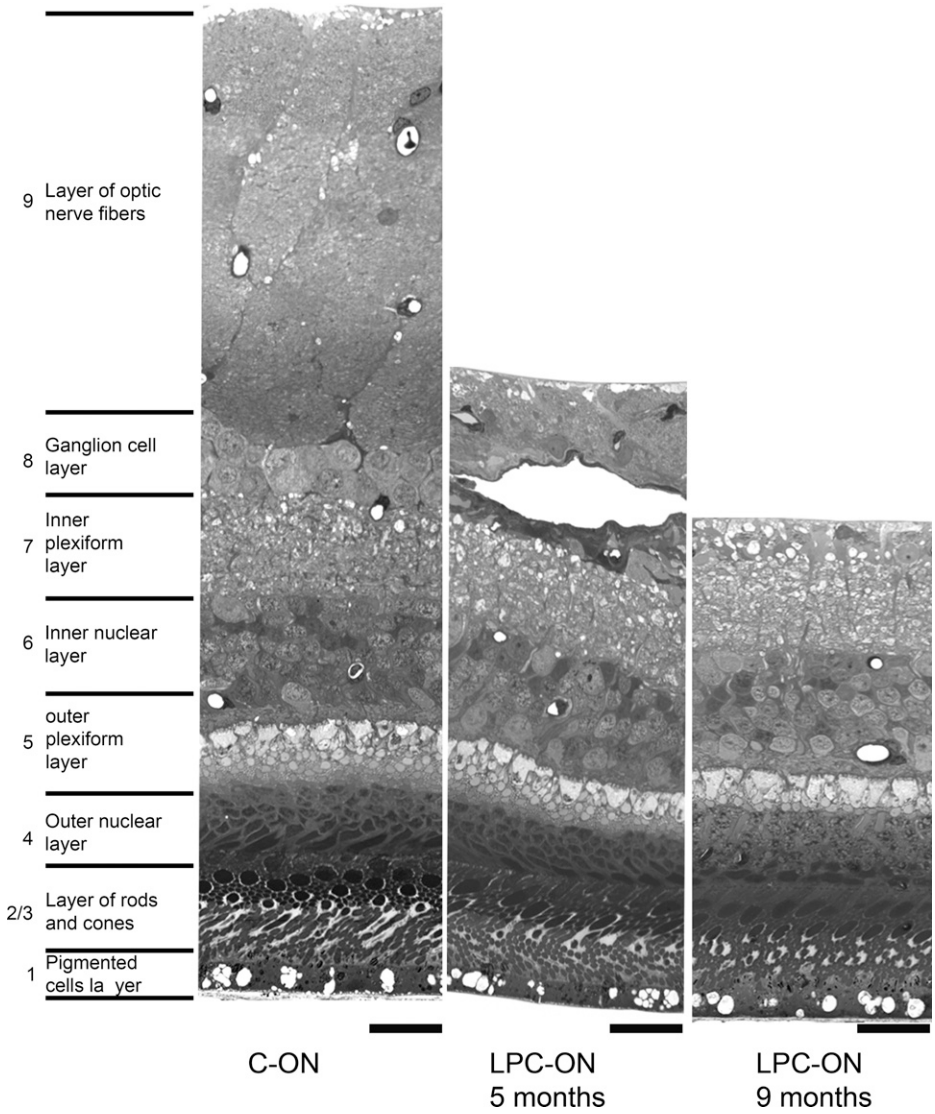

Fig. 8. Analysis of the LPC-induced retinal modifications on semithin cross-sections: progressive decrease of the retinal layers 8 and 9, at 5 and 9 mo post-LPC compared to the C-ON retinal layers. (Scale bar, 25 μm.)

accounted for environmental modifications, such as astrogliosis and glial-axon densities that were prominent in the LPC-ON and corresponding retina at later time-points. These increased membrane relationships between axons and glia are characteristics of persisting demyelination in chronic experimental autoimmune encephalomyelitis (EAE) (optic nerve and spinal cord) and MS plaques (spinal cord) (34, 35), and may confer a supportive role of glial cells to axons, thus representing a compensatory mechanism to the impaired nerve fiber conduction (34, 36).

As RGC project into the optic nerve, we questioned the consequence of optic nerve demyelination on the retina. SD-OCT on two subjects highlighted thinning of the RNFL at 3 and 5 mo, with no significant differences between the two time points, and retinal thinning was further validated by a decrease in RGC densities and retinal axons at the immuno-histological level, and thinning of the inner retinal layers at the ultrastructural level. SD-OCT is a noninvasive method of choice to track neuronal-axonal loss, and has provided evidence for injury to the inner retinal layers, including the RNFL and reduction of RGC cell density in MS patients (37). Our model thus validates that RNFL thinning reflects both neuronal and axonal loss. Retinal thinning occurs in MS with (38) or without optic neuritis (39), and as early as 6 mo after the first optic neuritis episode (38). The timeline of retinal damages in the macaque model is nearly comparable to man when adjusting macaque's mean life-duration to man. Interestingly, RNFL thinning was not observed in conditions of optic nerve hypomyelination in dogs (23), raising the question of RNFL thinning being a primary or secondary event to optic nerve demyelination. Our data showing that a primary event of optic nerve demyelination leading to optic nerve axonal loss is followed by RNFL thinning as seen by OCT and histological evaluation, corroborates the hypothesis that an optic nerve insult can be the cause of retinal pathology.

ERG predicted sparing of the outer retinal layers, a finding that was also confirmed at the immuno-histological and ultrastructural levels, thus indicating that the optic nerve induced demyelination has spared rods and cones. ERGs are often affected in MS (40) and could result either from retrograde transsynaptic degeneration of the retinal outer layers secondary to optic nerve atrophy or, for a small patient subset, retinal autoimmunity as a possible mechanism of degeneration (7). Although in the nonhuman primate model, ERGs were normal and sparing of the retinal outer layer was validated by electron microscopy, the possibility that transsynaptic degeneration of

the outer retinal layers leading to altered ERG could occur at later times cannot be excluded.

Although remyelination onsets during the first month postdemyelination in the nonhuman primate optic nerve (28), our present study indicates that it is compromised over time. Reasons for this failure could be multiple. While in rodents, remyelination is achieved successfully after acute demyelination, even in the optic nerve, it relies on oligodendrocyte progenitor proliferation, recruitment, and differentiation into mature oligodendrocytes (41). This initial burst in oligodendrocytes did not occur in the present model (28), sustaining its similarity with MS chronic lesions (42–44) and experimental models of chronic demyelination (45, 46). Although depleted in numbers, mature and immature oligodendrocytes were seen within lesions up to 9 mo postdemyelination. Both the slow tempo of differentiation of primate oligodendroglial cells (47–49) and their lack of proliferation, possibly caused by delayed astrocyte recruitment (28), could have prevented oligodendrocyte timely differentiation into myelin-forming cells. Moreover, noxious inflammatory conditions sustained by myeloid cells (monocytes and microglia), known to modulate remyelination (15), could also have blocked oligodendrocyte maturation as demonstrated for rodent and human oligodendrocytes (50–53). While at early stages macrophages/microglial cells were widely spread within the optic nerve lesions, they became restricted to the lesion rim at later stages, as observed in chronic or inactive MS lesions (54). Although present at early times, they may have failed to switch in a timely manner from a pro- to an antiinflammatory phenotype to allow remyelination to proceed (55, 56).

Failed remyelination was associated with progressive axonal loss and RGC degeneration. Although axons, were present in fair amounts and appeared healthy up to 2 mo postdemyelination (28) (*SI Appendix*, Fig. S6), their number decreased severely from 3 mo on (present study) with no significant differences among animals and correlating with optic nerve shrinkage. At the ultrastructural level, surviving axons remained anatomically normal up to 3 mo but were characterized thereafter (5 mo) by a number of cytoplasmic anomalies, including increased axonal organelles, loss of NF spacing, and microtubules as described for chronic MS lesions (57). While the cause of axonal loss and degeneration and their precise timing remain to be further investigated, sustained inadequate inflammation, glutamate excitotoxicity, and reduced oligodendroglial trophic support to axons (1, 57), may all have contributed to the progressive axon degeneration and evolution of the lesion from an early active state with remyelination onset, to a late chronic state with failed remyelination, neurodegeneration, and neurological dysfunction, mimicking the many features of MS chronic lesions (1, 57–59).

Conclusion

Although this nonhuman primate model of optic nerve demyelination does not represent the autoimmune component of MS, or its correlated preclinical model EAE, it has the obvious advantage to target the optic nerve in a very predictive manner, with demyelination followed by the onset of remyelination at early time points and failed remyelination, and axonal loss and visual dysfunction at late time points. The present model could provide a platform to improve our understanding of the mechanisms underlying axon pathology progression and failed remyelination. Moreover, the existence of a correlation between the functional assays and the structural/anatomical observations makes this model an excellent tool to develop strategies aiming at promoting neuroprotection and remyelination, to overcome the inevitable neurological disabilities of myelin diseases, such as MS.

Materials and Methods

Animals. Adult male *Macaca fascicularis* monkeys (5 to 10 y old) were purchased from and raised by Silabe, Strasbourg, or Bioprim, Perpignan, France, and hosted for the time of the experiments at the Institut du Cerveau primate facility. For ethical reasons, the number of animals ($n = 6$) was kept as minimal as possible following the legal requirements. The identification codes refer to individual monkeys (*SI Appendix*, Table S1). During quantification, animals had another code preventing the experimenter from identifying the animals. Experiments were performed according to European Community regulations and INSERM Ethical Committee (authorization 75-348; 20/04/2005) and approved by the local Darwin ethical and National committees (authorization #3469, and #17101).

Demyelination. LPC injection was performed in one optic nerve, the other optic nerve serving as control. Saline injection was reported to have minimal impact on demyelination and axon loss compared to LPC injection (28). Details can be found in *SI Appendix, SI Methods*.

Electroretinogram. ERG recordings were performed under anesthesia, with a Visiosystem (SIEM BIO MEDICALE) before (baseline) and after surgery. Data are the mean of three to four animals. The method for ERG recordings is described in detail in *SI Appendix, SI Methods*.

Pupillary Light Reflex. Changes in PLR parameters, such as constriction amplitude and latency, have been associated with retinal dysfunction, including degeneration of the rod and cone photoreceptors, and melanopsin-containing ganglion cells. The constriction and dilatation of the pupil in response to changes in light intensity were evoked and collected on awake animals by a portable Biovision device (SIEM BIO MEDICALE) equipped with an infrared-sensitive camera delivering continuous infrared illumination generating pupil images at 60 frames per second. Details are provided in *SI Appendix, SI Methods*.

Visual Evoked Potential. VEP recordings were performed in a dark room, using the MetroVision system, on awake animals using checkerboard and flash stimulations (750 ms) delivered bi- and monocularly averaging 60 sweeps per trial. Stimuli were 1 to 2 Hz. D15′ and D30′ checkerboard and red and blue flash responses were selected over D60′ and gray flash respectively, as the most sensitive and reliable parameters of follow-up throughout the study. Details can be found in *SI Appendix, SI Methods*.

Visual Field. VF sensitivity was indirectly assessed before and after the lesion using saccadic responses to targets presented successively in the VF. This procedure was used in monocular and binocular conditions with awake monkeys placed at 60 cm from a CRT screen, trained and rewarded to make saccades to visual targets using the Jeda in-house software (60). Details are provided in *SI Appendix, SI Methods*.

Optical Coherence Tomography. OCT imaging was performed on a spectral-domain iVue (software v3.2; Optovue) and was conducted under anesthesia in two animals after appropriate dilatation by Tropicamide 0.5% (Mydriaticum, Farmila-thea Farmaceutici). The detailed method can be found in *SI Appendix, SI Methods*.

Tissue Processing. Animals were killed by deep anesthesia at 3 ($n = 2$), 5 ($n = 2$), and 9 ($n = 2$) mo after LPC injection in the left optic nerve. The right optic nerve and retina were used as internal controls. Details are provided in *SI Appendix, SI Methods*.

Immunohistochemical and Ultrastructural Quantifications. Quantifications were performed as described in details in *SI Appendix, SI Methods*. Statistics were performed as described in *SI Appendix, SI Methods*.

Data Availability. All study data are included in the main text and *SI Appendix*.

ACKNOWLEDGMENTS. We thank Morgane Weissenburger, Marion Lanoe, Harry Ahnine, Oceane Aribo, and Serban Morosan (Institut du Cerveau Primate Facility), Dominique Langui (Institut du Cerveau Imaging Facility), as well as Fabrice Arcizet and Celine Nouvel-Jaillard (Institut de la Vision) for their valuable operational contributions and support; Dr. A. Green and members of his team for helpful discussions; and Dr. S. Mozafari for her valuable advice on remyelination assessment. This work was supported by the programs 'Institut des Neurosciences Translationnelles' ANR-10-IAIHU-06, the International Associated Laboratory "Neuro-Bridge," and the NIH/National Institute of Neurological Disorders and Stroke SR01NS105741-02.

1. B. D. Trapp, K.-A. Nave, Multiple sclerosis: An immune or neurodegenerative disorder? *Annu. Rev. Neurosci.* **31**, 247–269 (2008).
2. E. Frohman *et al.*, Optical coherence tomography in multiple sclerosis. *Lancet Neurol.* **5**, 853–863 (2006).
3. D. L. Arnold, Changes observed in multiple sclerosis using magnetic resonance imaging reflect a focal pathology distributed along axonal pathways. *J. Neurol.* **252** (suppl. 5), v25–v29 (2005).
4. L. J. Balk *et al.*, Timing of retinal neuronal and axonal loss in MS: A longitudinal OCT study. *J. Neurol.* **263**, 1323–1331 (2016).
5. S. Ortiz-Perez *et al.*, Visual field impairment captures disease burden in multiple sclerosis. *J. Neurol.* **263**, 695–702 (2016).
6. J. de Seze *et al.*, Pupillary disturbances in multiple sclerosis: Correlation with MRI findings. *J. Neurol. Sci.* **188**, 37–41 (2001).
7. F. Forooghian *et al.*, Electroretinographic abnormalities in multiple sclerosis: Possible role for retinal autoantibodies. *Doc. Ophthalmol.* **113**, 123–132 (2006).
8. C. Cordano *et al.*, pRNFL as a marker of disability worsening in the medium/long term in patients with MS. *Neurol. Neuroimmunol. Neuroinflamm.* **6**, e533 (2018).
9. A. Brusa, S. J. Jones, G. T. Plant, Long-term remyelination after optic neuritis: A 2-year visual evoked potential and psychophysical serial study. *Brain* **124**, 468–479 (2001).
10. I. P. Chatziralli, M. M. Moschos, D. Brouzas, K. Kopsidas, I. D. Ladas, Evaluation of retinal nerve fibre layer thickness and visual evoked potentials in optic neuritis associated with multiple sclerosis. *Clin. Exp. Optom.* **95**, 223–228 (2012).
11. A. J. Green *et al.*, Clemastine fumarate as a remyelinating therapy for multiple sclerosis (ReBUILD): A randomised, controlled, double-blind, crossover trial. *Lancet* **390**, 2481–2489 (2017).
12. S. Picaud *et al.*, The primate model for understanding and restoring vision. *Proc. Natl. Acad. Sci. U.S.A.* **116**, 26280–26287 (2019).
13. K. Chanoumidou, S. Mozafari, A. Baron-Van Evercooren, T. Kuhlmann, Stem cell derived oligodendrocytes to study myelin diseases. *Glia* **68**, 705–720 (2020).
14. S. Mozafari, A. Baron-Van Evercooren, Human stem cell-derived oligodendrocytes: From humanized animal models to cell therapy in myelin diseases. *Semin. Cell Dev. Biol.* **116**, 53–61 (2021).
15. R. J. M. Franklin, C. Ffrench-Constant, Regenerating CNS myelin—From mechanisms to experimental medicines. *Nat. Rev. Neurosci.* **18**, 753–769 (2017).
16. G. S. Melchor, T. Khan, J. F. Reger, J. K. Huang, Remyelination pharmacotherapy investigations highlight diverse mechanisms underlying multiple sclerosis progression. *ACS Pharmacol. Transl. Sci.* **2**, 372–386 (2019).
17. R. M. Bove, A. J. Green, Remyelinating pharmacotherapies in multiple sclerosis. *Neurotherapeutics* **14**, 894–904 (2017).
18. Y. Kondo *et al.*, Spontaneous optic nerve compression in the osteopetrotic (op/op) mouse: A novel model of myelination failure. *J. Neurosci.* **33**, 3514–3525 (2013).
19. S. Mozafari, M. A. Sherafat, M. Javan, J. Mirnajafi-Zadeh, T. Tiraihi, Visual evoked potentials and MBP gene expression imply endogenous myelin repair in adult rat optic nerve and chiasm following local lysolecithin induced demyelination. *Brain Res.* **1351**, 50–56 (2010).
20. L. Schirmer *et al.*, Oligodendrocyte-encoded Kir4.1 function is required for axonal integrity. *eLife* **7**, e36428 (2018).
21. Y. You, A. Klistorner, J. Thie, S. L. Graham, Latency delay of visual evoked potential is a real measurement of demyelination in a rat model of optic neuritis. *Invest. Ophthalmol. Vis. Sci.* **52**, 6911–6918 (2011).
22. M. Heidari *et al.*, Evoked potentials as a biomarker of remyelination. *Proc. Natl. Acad. Sci. U.S.A.* **116**, 27074–27083 (2019).
23. L. B. C. Teixeira *et al.*, Modeling the chronic loss of optic nerve axons and the effects on the retinal nerve fiber layer structure in primary disorder of myelin. *Invest. Ophthalmol. Vis. Sci.* **57**, 4859–4868 (2016).
24. L. Satarian *et al.*, Engrafted human induced pluripotent stem cell-derived anterior specified neural progenitors protect the rat crushed optic nerve. *PLoS One* **8**, e71855 (2013).
25. S. Dehghan, M. Javan, F. Pourabdolhossein, J. Mirnajafi-Zadeh, H. Baharvand, Basic fibroblast growth factor potentiates myelin repair following induction of experimental demyelination in adult mouse optic chiasm and nerves. *J. Mol. Neurosci.* **48**, 77–85 (2012).
26. A. Cruz-Herranz *et al.*, Monitoring retinal changes with optical coherence tomography predicts neuronal loss in experimental autoimmune encephalomyelitis. *J. Neuroinflammation* **16**, 203 (2019).
27. A. Moshiri *et al.*, A nonhuman primate model of inherited retinal disease. *J. Clin. Invest.* **129**, 863–874 (2019).
28. F. Lachapelle *et al.*, Failure of remyelination in the nonhuman primate optic nerve. *Brain Pathol.* **15**, 198–207 (2005).
29. I. D. Duncan *et al.*, The adult oligodendrocyte can participate in remyelination. *Proc. Natl. Acad. Sci. U.S.A.* **115**, E11807–E11816 (2018).
30. S. Jäkel *et al.*, Altered human oligodendrocyte heterogeneity in multiple sclerosis. *Nature* **566**, 543–547 (2019).
31. C. M. Bacmeister *et al.*, Motor learning promotes remyelination via new and surviving oligodendrocytes. *Nat. Neurosci.* **23**, 819–831 (2020).
32. Y. Tomiyama *et al.*, Measurement of electroretinograms and visually evoked potentials in awake moving mice. *PLoS One* **11**, e0156927 (2016).
33. P. Sriram *et al.*, Relationship between optical coherence tomography and electrophysiology of the visual pathway in non-optic neuritis eyes of multiple sclerosis patients. *PLoS One* **9**, e102546 (2014).
34. D. Soffer, C. S. Raine, Morphologic analysis of axo-glial membrane specializations in the demyelinated central nervous system. *Brain Res.* **186**, 301–313 (1980).
35. C. K. Henrikson, J. E. Vaughn, Fine structural relationships between neurites and radial glial processes in developing mouse spinal cord. *J. Neurocytol.* **3**, 659–675 (1974).
36. C. S. Raine, Membrane specialisations between demyelinated axons and astroglia in chronic EAE lesions and multiple sclerosis plaques. *Nature* **275**, 326–327 (1978).
37. A. J. Green, S. McQuaid, S. L. Hauser, I. V. Allen, R. Lyness, Ocular pathology in multiple sclerosis: Retinal atrophy and inflammation irrespective of disease duration. *Brain* **133**, 1591–1601 (2010).
38. I. Gabilondo *et al.*, Dynamics of retinal injury after acute optic neuritis. *Ann. Neurol.* **77**, 517–528 (2015).
39. S. B. Syc *et al.*, Optical coherence tomography segmentation reveals ganglion cell layer pathology after optic neuritis. *Brain* **135**, 521–533 (2012).
40. D. Papakostopoulos, F. Fotiou, J. C. Hart, N. K. Banerji, The electroretinogram in multiple sclerosis and demyelinating optic neuritis. *Electroencephalogr. Clin. Neurophysiol.* **74**, 1–10 (1989).
41. R. J. Franklin, C. Ffrench-Constant, Remyelination in the CNS: From biology to therapy. *Nat. Rev. Neurosci.* **9**, 839–855 (2008).
42. G. Wolswijk, Chronic stage multiple sclerosis lesions contain a relatively quiescent population of oligodendrocyte precursor cells. *J. Neurosci.* **18**, 601–609 (1998).
43. A. Chang, W. W. Tourtellotte, R. Rudick, B. D. Trapp, Premyelinating oligodendrocytes in chronic lesions of multiple sclerosis. *N. Engl. J. Med.* **346**, 165–173 (2002).
44. T. Kuhlmann *et al.*, Differentiation block of oligodendroglial progenitor cells as a cause for remyelination failure in chronic multiple sclerosis. *Brain* **131**, 1749–1758 (2008).
45. H. S. Keirstead, J. M. Levine, W. F. Blakemore, Response of the oligodendrocyte progenitor cell population (defined by NG2 labelling) to demyelination of the adult spinal cord. *Glia* **22**, 161–170 (1998).
46. E. S. Johnson, S. K. Ludwin, The demonstration of recurrent demyelination and remyelination of axons in the central nervous system. *Acta Neuropathol.* **53**, 93–98 (1981).
47. M. Ehrlich *et al.*, Rapid and efficient generation of oligodendrocytes from human induced pluripotent stem cells using transcription factors. *Proc. Natl. Acad. Sci. U.S.A.* **114**, E2243–E2252 (2017).
48. D. Buchet, C. Garcia, C. Deboux, B. Nait-Oumesmar, A. Baron-Van Evercooren, Human neural progenitors from different foetal forebrain regions remyelinate the adult mouse spinal cord. *Brain* **134**, 1168–1183 (2011).
49. S. Mozafari *et al.*, Multiple sclerosis iPS-derived oligodendroglia conserve their properties to functionally interact with axons and glia in vivo. *Sci. Adv.* **6**, abc6983 (2020).
50. I. E. Morales Pantoja *et al.*, iPSCs from people with MS can differentiate into oligodendrocytes in a homeostatic but not an inflammatory milieu. *PLoS One* **15**, e0233980 (2020).
51. L. Starost *et al.*, Extrinsic immune cell-derived, but not intrinsic oligodendroglial factors contribute to oligodendroglial differentiation block in multiple sclerosis. *Acta Neuropathol.* **140**, 715–736 (2020).
52. L. Kirby *et al.*, Oligodendrocyte precursor cells present antigen and are cytotoxic targets in inflammatory demyelination. *Nat. Commun.* **10**, 3887 (2019).
53. M. El Behi *et al.*, Adaptive human immunity drives remyelination in a mouse model of demyelination. *Brain* **140**, 967–980 (2017).
54. K. Heß *et al.*, Lesion stage-dependent causes for impaired remyelination in MS. *Acta Neuropathol.* **140**, 359–375 (2020).
55. A. F. Lloyd *et al.*, Central nervous system regeneration is driven by microglia necroptosis and repopulation. *Nat. Neurosci.* **22**, 1046–1052 (2019).
56. V. E. Miron, Beyond immunomodulation: The regenerative role for regulatory T cells in central nervous system remyelination. *J. Cell Commun. Signal.* **11**, 191–192 (2017).
57. R. Dutta, B. D. Trapp, Mechanisms of neuronal dysfunction and degeneration in multiple sclerosis. *Prog. Neurobiol.* **93**, 1–12 (2011).
58. S. Luchetti *et al.*, Progressive multiple sclerosis patients show substantial lesion activity that correlates with clinical disease severity and sex: A retrospective autopsy cohort analysis. *Acta Neuropathol.* **135**, 511–528 (2018).
59. T. Kuhlmann, G. Lingfeld, A. Bitsch, J. Schuchardt, W. Brück, Acute axonal damage in multiple sclerosis is most extensive in early disease stages and decreases over time. *Brain* **125**, 2202–2212 (2002).
60. J. Lorenceau, R. Humbert, A multipurpose software package for editing two-dimensional animated images *Behav. Res. Methods Instrum. Comput.* **22**, 453–465 (1990).